A novel shape sensing approach based on the coupling of Modal Virtual Sensor Expansion and iFEM:
Numerical and experimental assessment on composite stiffened structures

(Article begins on next page)
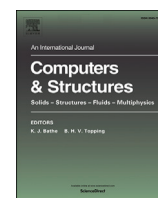
A novel shape sensing approach based on the coupling of Modal Virtual Sensor Expansion and iFEM: Numerical and experimental assessment on composite stiffened structures

Marco Esposito

Department of Mechanical and Aerospace Engineering, Politecnico di Torino, Corso Duca degli Abruzzi, 24, 10129 Torino, Italy

ARTICLE INFO

ABSTRACT

Shape sensing, i.e. the reconstruction of the displacement field of a structure from discrete strain measurements, is becoming crucial for the development of a modern Structural Health Monitoring framework. Nevertheless, an obstacle to the affirmation of shape sensing as an efficient monitoring system for existing structures is represented by its requirement for a significant amount of sensors. Two shape sensing methods have proven to exhibit complementary characteristics in terms of accuracy and required sensors that make them suitable for different applications, the inverse Finite Element Method (iFEM) and the Modal Method (MM). In this work, the formulations of these two methods are coupled to obtain an accurate shape sensing approach that only requires a few strain sensors. In the proposed procedure, the MM is used to virtually expand the strains coming from a reduced number of strain measurement locations. The expanded set of strains is then used to perform the shape sensing with the iFEM. The proposed approach is numerically and experimentally tested on the displacement reconstruction of composite stiffened structures. The results of these analyses show that the formulation is able to strongly reduce the number of required sensors for the iFEM and achieve an extremely accurate displacement reconstruction.

1. Introduction

Shape sensing is defined as the reconstruction of the deformed shape of a structure from discrete strain measurements. This technique is rapidly imposing its importance for the development of a modern Structural Health Monitoring (SHM) framework. In fact, the continuous monitoring of the displacements during the service life can provide crucial information on the health status of a structure, allowing the detection of damages and efficiently guiding the maintenance operations [1–8]. In addition, the shape sensing can work as a feedback monitoring system for the control of the morphing mechanism of the recently developed smart structures [9,10].

Several shape sensing methods have been proposed during the last two decades. They are all based on the computation of the displacement field from discrete strain measurements, but they differ in the working principle that they are based on. In the present work, two shape sensing methods are considered due to their success in the open literature, the inverse Finite Element Method (iFEM) and the Modal Method (MM).

The iFEM, firstly formulated in [11], is based on the discretisation of the structural domain with finite elements and on the consequent approximation of the strain field in terms of nodal degrees of freedom (displacements and rotations) and shape functions. The error between this analytical strain field and the one measured at some discrete locations is then minimised in order to compute the values of nodal degrees of freedom that best fit the measured strains. The iFEM has been successfully applied to the analysis of beam-like structures [12–14], of thin walled structures [15,16] and of sandwich and multilayered composite structures [17–20]. Recently, the modelling capabilities of the method have been enhanced with the use of isogeometric formulations [21,22]. Moreover, in [23], iFEM has been extended to achieve damage detection through the reconstruction of the modal parameters of plate structures. Damage detraction for multilayered plates has also been investigated in [24], with the introduction of refined zigzag theory (RZT) within the iFEM framework.

The MM is based on the approximation of the strain field in terms of known spatial functions, the modal strain shapes, and unknown weights, the modal coordinates. The modal coordinates are computed by fitting the so-formulated strain field to the discretely measured strains. The displacement field is then computed by means of the strain-displacement relations. The Modal Method has been introduced in [25,26] and applied

to the analysis of plates in [27,28]. Recently, the MM has also been applied to the static and dynamic analysis of a wing experiencing small [29] and large deformations [30].

Although recent developments have been introduced in the strain sensing technology [31,32], the availability of a sufficient number of strain measurements for the shape sensing methods is an ongoing issue, especially for the already designed structures that are instrumented with few strain sensors. In this regard, the comparative studies in [33,34] discuss the relative merits and drawbacks of the iFEM and the MM. In fact, the iFEM shows superior accuracy in the reconstruction of the displacement field, but at the cost of a large number of strain sensors. On the other hand, the MM is able of a decent accuracy with sparse sensor configurations, but it is not able to reach the accuracy of the iFEM, even with a significant number of sensors. Few studies have been performed on the virtual extrapolation of strains from a few sensors to feed the iFEM with more strain information. In [35], the Smoothing Element Analysis (SEA) was introduced as a finite element based approach able to interpolate, with a controllable degree of smoothness, single stress components over a specific domain. The SEA has been extended to the interpolation of strain components and, coupled with the iFEM, has been used for the experimental shape sensing of a wing-shape sandwich laminate [36] and, recently, for the numerical shape sensing of an aluminium plate [37]. The polynomial fitting has been also adopted for the same purpose in [38]. More recently, in [39], the performance of SEA and polynomial fitting have been compared for the experimental case of a composite plate subject to buckling. Despite their successful applications, these pre-extrapolation techniques can only be applied to simple geometries. In fact, they can expand the strain field to parts of the structural domain that belong to the same surface of the measured strains, i.e. for a stiffened panel, strains measured on the skin can not be used to extrapolate strains on the stiffeners and vice versa. Moreover, these methods can only be applied to scalar quantities and, therefore, the strain field needs to be extrapolated performing a separate procedure for each component.

In this work, a method that combines the iFEM and MM's working principles to overcome the limitations of the two methods is proposed. The MM, thanks to its adaptably to sparse strain sensors' configuration, is adopted as a Virtual Sensor Expansion (VSE) method for the pre-extrapolation to a large number of strain information from a small amount of measured strains. This pre-extrapolation technique overcomes the limitation on the extrapolation domain highlighted for the SEA and the polynomial fitting. The iFEM is then fed with the expanded set of strains, thus allowing it to process a sufficient amount of strain information. This procedure is tested on the numerical and experimental shape sensing of stiffened multilayered composite structures. The study shows that the mixing of the two methods is able to overcome the limitations of their separate application. In fact, the results prove that the methodology can reconstruct a highly accurate displacement field, even when using a reduced number of strain sensors.

The paper is structured as follows. In Section 2, the MM and the iFEM are introduced. In Section 3, the proposed method that combines the two previously described shape sensing methods is formulated. In Section 4, the numerical experiment is described. The results of this investigation are reported in Section 5. The experimental validation of the introduced method is described in Section 6. Finally, the concluding remarks are presented in Section 7.

2. Shape sensing methods

In the following section, the inverse Finite Element Method (iFEM) and the Modal Method (MM) are summarised in order to set the numerical framework for the novel approach. In particular, the formulation is presented for the case of thin-walled structures, thus two-dimensional inverse finite elements are considered. Nevertheless, the proposed approach is easily applicable to beam and frame structures by using one-dimensional inverse elements.
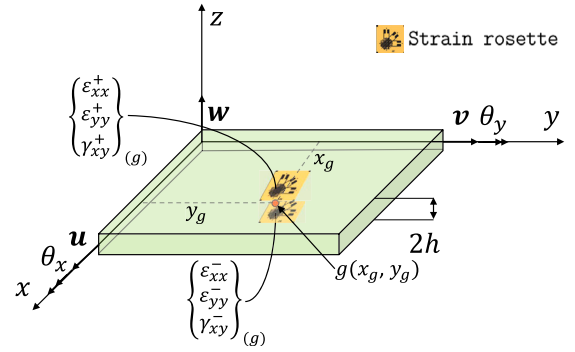

Fig. 1. Plate - The figure shows the notation of the plate's kinematic variables and the strain sensor's back-to-back configuration for the computation of the membrane strain measures and of the bending curvatures in the g-th location.

2.1. iFEM

The inverse Finite Element Method is based on the discretisation of the structural domain with finite elements. As for the standard/direct Finite Element Method, the displacement field within each element is interpolated using unknown nodal degrees of freedom and known spatial shape functions [40]. The strain field is then easily expressed in terms of the spatial derivatives of the shape functions and of the nodal degrees of freedom [41]. Considering the First-order Shear Deformation Theory as the kinematic model for a thin plate, the strain field (three in-plane strain components and two transverse shear strain components) can be expressed in terms of eight strain measures, ε_k ($k = 1, 2, ..., 8$):

$$\begin{Bmatrix} \varepsilon_{xx} \\ \varepsilon_{yy} \\ \gamma_{xy} \end{Bmatrix} = \begin{Bmatrix} u_{,x} \\ v_{,x} \\ v_{,x} + u_{,y} \end{Bmatrix} + z \begin{Bmatrix} \theta_{y,x} \\ -\theta_{x,y} \\ (\theta_{y,y} - \theta_{x,x}) \end{Bmatrix} = \begin{Bmatrix} \varepsilon_1 \\ \varepsilon_2 \\ \varepsilon_3 \end{Bmatrix} + z \begin{Bmatrix} \varepsilon_4 \\ \varepsilon_5 \\ \varepsilon_6 \end{Bmatrix} = \boldsymbol{e} + z\boldsymbol{k}$$
(1a)

$$\begin{Bmatrix} \gamma_{xz} \\ \gamma_{yz} \end{Bmatrix} = \begin{Bmatrix} w_{,x} + \theta_y \\ w_{,y} - \theta_x \end{Bmatrix} = \begin{Bmatrix} \varepsilon_7 \\ \varepsilon_8 \end{Bmatrix} = \boldsymbol{g}$$
(1b)

where $\boldsymbol{e}$ are the membrane strain measures, $\boldsymbol{k}$ are the bending curvatures and $\boldsymbol{g}$ are the transverse-shear strain measures. The kinematic variables u, v, w, θ_x, θ_y and the coordinate z, relative to a generic plate, are illustrated in Fig. 1.

The introduction of a FE discretisation of the structural domain leads to the interpolation of the kinematic variables, within each finite element, in terms of the shape functions' matrix, $\mathbf{N}$, and of the vector of the nodal degrees of freedoms (DOFs), $\mathbf{u}^e$:

$$[u, v, w, \theta_x, \theta_y]^T = \mathbf{N}\mathbf{u}^e$$
(2)

The eight strain measures defined in Eq. (1) can be then expressed in terms of the nodal DOFs as follows:

$$\varepsilon_k(\mathbf{u}^e) = \mathbf{B}_k \mathbf{u}^e \quad (k = 1, 2, ..., 8)$$
(3)

where $\mathbf{B}_k$ is the matrix containing the spatial derivatives of the shape functions corresponding to the k-th strain measure.

The objective of the iFEM is to find the nodal DOFs that best fit, in a least-squares sense, the analytic strain measures (3) with those experimentally evaluated at some discrete locations on the structure. This is obtained by minimising the error between the analytical and the measured strain measures expressed by the following functional:

$$\Psi^e(\mathbf{u}^e) = \sum_{k=1}^{8} \lambda_k^e w_k^e \iint_{A^e} (\varepsilon_k(\mathbf{u}^e) - \varepsilon_k^m)^2 \, dx \, dy$$
(4)

In the functional, ε_k^m denotes the k-th strain measure experimentally evaluated on the structure and A^e is the area of the inverse element. w_k^e are coefficients used to guarantee the dimensional consistency between

the different addenda of the functional. They are set as follows: $w_k^e = 1$ for $k = 1, 2, 3, 7, 8$ and $w_k^e = (2h)^2$ for $k = 4, 5, 6$, where h is the half-thickness of the element. On the other hand, λ_k^e are coefficients used to take into account for the sparsity of the experimentally evaluated strain measures. They are set as follows: $\lambda_k^e = 1$ if the k-th strain measure is actually measured, or to a small value $\lambda_k^e = (10^{-4}, 10^{-5}, 10^{-6})$ if the corresponding strain measure is not measured. In this case, the corresponding ε_k^m is set to 0.

The first six strain measures that appear in Eq. (4) can be experimentally evaluated (^{m}), at a generic (g) location, from strain sensors located on the bottom surface (-) and on the top (+) surface of a plate through the computation of the membrane strains and the bending curvatures:

$$\mathbf{e}_{(g)}^m = \begin{Bmatrix} \varepsilon_1^m \\ \varepsilon_2^m \\ \varepsilon_3^m \end{Bmatrix}_{(g)} = \frac{1}{2} \begin{Bmatrix} \varepsilon_{xx}^+ + \varepsilon_{xx}^- \\ \varepsilon_{yy}^+ + \varepsilon_{yy}^- \\ \gamma_{xy}^+ + \gamma_{xy}^- \end{Bmatrix}_{(g)} \tag{5a}$$

$$\mathbf{k}_{(g)}^m = \begin{Bmatrix} \varepsilon_4^m \\ \varepsilon_5^m \\ \varepsilon_6^m \end{Bmatrix}_{(g)} = \frac{1}{2h} \begin{Bmatrix} \varepsilon_{xx}^+ - \varepsilon_{xx}^- \\ \varepsilon_{yy}^+ - \varepsilon_{yy}^- \\ \gamma_{xy}^+ - \gamma_{xy}^- \end{Bmatrix}_{(g)} \tag{5b}$$

Fig. 1 illustrates the use of a strain rosette to compute these six strain measures. By using unidirectional sensors, only the corresponding strain measures can be computed and the penalisation scheme based on the λ_k^e is adopted for the remaining strain measures. Differently, the transverse shear strain measures (ε_7 and ε_8, (Eq. (1))), can never be experimentally evaluated. Therefore, the $\lambda_{7,8}^e$ are always set to a small value $(10^{-4}, 10^{-5}, 10^{-6})$ and the $\varepsilon_{7,8}^m$ are set to 0.

Once the functional is defined, it can be minimised to compute the DOFs that best fit, in a least-squares sense, the measured strain field at the sensorised locations. The minimisation of Eq. (4) leads to a system of algebraic linear equations:

$$\frac{\partial \Psi_e(\mathbf{u}^e)}{\partial \mathbf{u}^e} = \mathbf{l}^e \mathbf{u}^e - \mathbf{f}^e = 0 \tag{6a}$$

$$\mathbf{u}^e = \mathbf{l}^{e-1} \mathbf{f}^e \tag{6b}$$

The assembly procedure, typical of the standard FEM, is then adopted to extend the procedure to all the elements of the structure. As a consequence, the assembly of the $\mathbf{l}^e$ matrices generates the global $\mathbf{L}$ matrix and the assembly of the $\mathbf{f}^e$ vectors generates the global $\mathbf{F}$ vector. The vector of the global DOFs, $\mathbf{U}$, can then be computed as:

$$\mathbf{U} = \mathbf{L}^{-1} \mathbf{F} \tag{7}$$

The penalisation scheme adopted in Eq. (4) allows the application of the method to structures with sparse strain sensors' configurations, i.e., with inverse elements that do not contain strain sensors. On the other hand, in some previous works [33,34], it has been highlighted that the method is only able to guarantee consistent accuracy for moderately sparse sensors' configuration, whereas it guarantees impressive accuracy for structures instrumented with a significant amount of sensors.

2.2. Modal method

The modal method is a shape sensing technique that uses the modal characteristics of a structure to derive its deformed shape from a set of discretely measured strains [25,28].

If a FE discretisation of a structural domain is considered, the vectors of the nodal degrees of freedom, $(\mathbf{w})_{D \times 1}$, and of the available strain components, $(\varepsilon)_{S \times 1}$, can be expressed in terms of the vector of the modal coordinates $(\mathbf{q})_{M \times 1}$:

$$\mathbf{w} = \mathbf{\Phi}_d \mathbf{q} \tag{8}$$

$$\varepsilon = \mathbf{\Phi}_s \mathbf{q} \tag{9}$$

where the modal matrix $(\mathbf{\Phi}_d)_{D \times M}$ is constituted by M columns (the i-th column being the i-th modal eigenvector of the degrees-of-freedom). The modal matrix $(\mathbf{\Phi}_s)_{S \times M}$ is also constituted by M columns (the i-th column being the i-th set of strains corresponding to the i-th mode shape of the FE model of the structure). The generalised formulation of the MM includes the case where the number of S measured strains is different from the number of M computed modes. In particular, this formulation considers the most common case where $S > M$. In this case, the displacements can be computed by pseudo-inverting Eq. (9) and substituting it into Eq. (8):

$$\mathbf{w} = \mathbf{\Phi}_d (\mathbf{\Phi}_s^T \mathbf{\Phi}_s)^{-1} \mathbf{\Phi}_s^T \varepsilon \tag{10}$$

thus allowing the computation of the discretised displacement field, expressed in terms of the modal shapes, that best fits the measured strains in a least-squares sense. The selection of the modes to be retained is crucial for the accuracy of the method. In [28] and [29], two criteria for the modes selection are described. Differently from the iFEM, the MM proved to be reasonably accurate in the reconstruction of the displacement field, even considering sparse strain sensors' configurations [33,34]. However, especially for deformed shapes that do not resemble any mode shape of the structure, the MM is not as accurate as the iFEM, even when a huge number of strain sensors is considered. This behaviour will be demonstrated in the following of the paper.

3. Modal Virtual Sensor Expansion coupled with iFEM

The shape sensing method proposed in this paper has the objective of combining the characteristics of the two previously described methods, the MM and the iFEM. The purpose is to overcome the limitation of the iFEM when sparse sensors' arrays are available, and, on the other hand, to exploit the adaptability of the MM to the same kind of applications. This mixing is obtained by a two-step procedure. The first step involves the Modal Virtual Sensor Expansion (Modal VSE) of a reduced number of strain measurements according to a formulation based on the same principle that the MM relies on. The expanded strain measures are then used in the second step as an input for the shape sensing through the iFEM.

In [42], O' Callahan et al. formulated the System Equivalent Reduction Expansion Process (SEREP). The process can be applied to the virtual expansion of a few strain measurements to a higher number. If we consider a vector of S strain components $(\varepsilon)_{S \times 1}$, it can be split into two subsets, one of S_m measured strains, $(\varepsilon^m)_{S_m \times 1}$, and one of S_e expanded strains, $(\varepsilon^e)_{S_e \times 1}$, where $S = S_m + S_e$:

$$\varepsilon = \begin{Bmatrix} \varepsilon^m \\ \varepsilon^e \end{Bmatrix} \tag{11}$$

The modal transformation described by Eq. (9) can be applied to both the subsets, thus resulting in:

$$\varepsilon^m = \mathbf{\Phi}_s^m \mathbf{q} \tag{12}$$

$$\varepsilon^e = \mathbf{\Phi}_s^e \mathbf{q} \tag{13}$$

where $\mathbf{\Phi}_s^m$ and $\mathbf{\Phi}_s^m$ are the modal strain matrices relative to the ε^m and the ε^e strains, respectively.

The pseudo inversion of Eq. (12) leads to

$$\mathbf{q} = [(\mathbf{\Phi}_s^m)^T \mathbf{\Phi}_s^m]^{-1} (\mathbf{\Phi}_s^m)^T \varepsilon^m \tag{14}$$

that substituted into Eq. (13) results in:

$$\varepsilon^e = \mathbf{\Phi}_s^e [(\mathbf{\Phi}_s^m)^T \mathbf{\Phi}_s^m]^{-1} (\mathbf{\Phi}_s^m)^T \varepsilon^m \tag{15}$$

This expression allows the computation of the ε^e subset of strains from the ε^m subset, and consequently, the knowledge of the full set of ε strains from the ε^m strains only. If we consider that ε^m is a set of actually measured strain components on a structure, Eq. (15) allows the expansion of these measurements to strains at different locations of the structure and
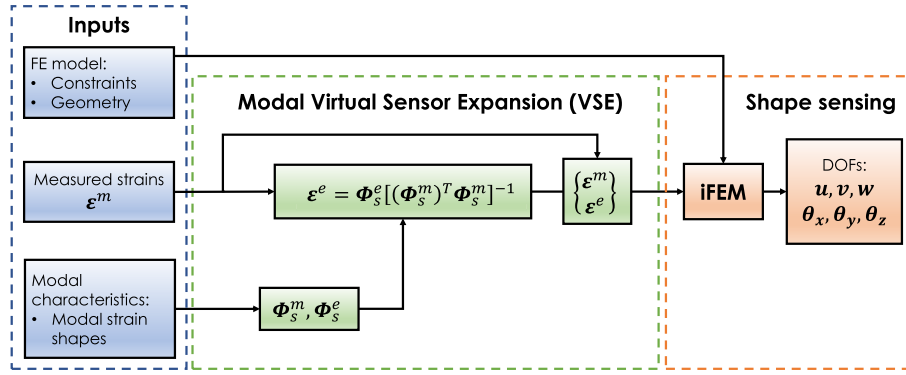
Fig. 2. Scheme of the two-step procedure that couples the Modal VSE and the iFEM.

to strains in different directions. In fact, since the modal strain shapes are defined over the whole structural domain and for the strain components in every direction, there is no limitation to the location and direction of the virtual expansion, i.e. from discrete strain components along a generic x-direction on a surface of a structure, strain components along the y-direction on a different surface of the same structure can be computed. This feature overcomes the limitation of other strain pre-extrapolation techniques, like Smoothing Element Analysis (SEA), that can only interpolate strain components in the same direction on the same surface. As for the MM, also for this technique, it is important to select representative modes to be retained in the formulation of $\mathbf{\Phi}_s$. The same criteria described in [28] and [29] can be used. Moreover, the number of considered modes (M) once again constraints the minimum number of measured strains that can be used, i.e. $S_m > M$.

Once the virtually expanded set of strains is obtained, it is used to perform shape sensing by means of the iFEM, as described in Section 2.1. This two-step procedure is schematised in Fig. 2.

The introduction of the Modal VSE prior to the application of iFEM will prove to be very beneficial in terms of reduction in the number of sensors for shape sensing. However, the Modal VSE introduces a requirement that is not necessary when simply applying standard iFEM, which is the knowledge of the material properties of the structure. In fact, the iFEM is based on the strain-displacement relationship that does not involve the material properties. On the contrary, Modal VSE relies on the computation of the modal characteristics of the structure, that depend on the material properties. Although material properties are often available in engineering problems, this aspect could limit the application of Modal VSE coupled with iFEM to applications where these properties are known.

4. Numerical case study

The introduced method is assessed with a numerical investigation regarding a composite stiffened panel, deformed under a concentrated force. This test case, which will be described in detail in the following sections, is of particular relevance to the approach presented in the current work. In fact, the shape-sensing analysis of the considered structure can reveal the limitations of the iFEM and the MM when used separately.

4.1. Test case

The test case is a composite stiffened panel of length L = 1000 mm and width W = 600 mm. It has three L-shaped stringers on one face, whereas the other face is flat. The geometry of the panel is presented in Figs. 3 and 4.

The whole panel, including the skin and the stiffeners, is made of composite laminates with the lamina characteristics summarised in Table 1. The lay-ups for the skins and the stringers are reported in Table 2. The stacking sequence is symmetric with respect to each component's mid-surface and the reference direction for the ply angles is shown in
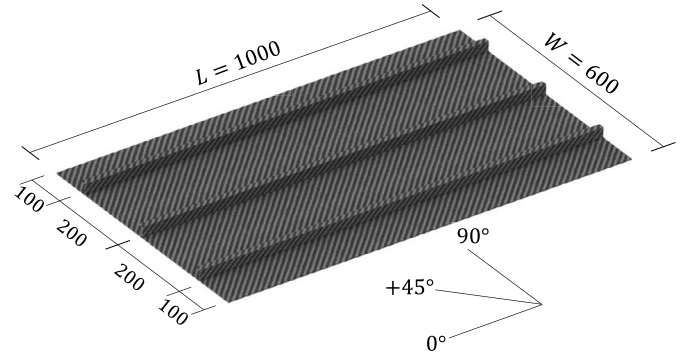

Fig. 3. Panel's geometry - The figure shows the geometry of the stiffened panel along with the reference directions for the composite stacking sequences (all dimensions are expressed in mm).
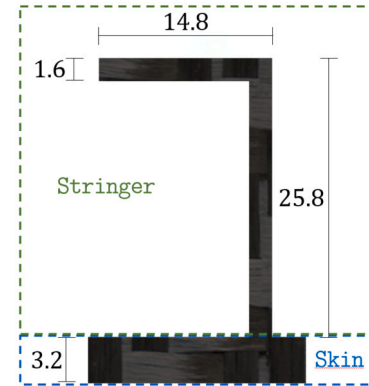

Fig. 4. Stinger and skin interface - The figure shows the geometry of the stringer and the thickness of the skin (all dimensions are expressed in mm).

Fig. 3. The directions are referred to the skin's lay-ups. The stringers' lay-ups are obtained by folding the plies from the skin. As a consequence, the reference directions result from this folding.

Two loading conditions are considered. Both configurations have clamping boundary conditions on the shorter edges of the panel, including the edges of the stringers in that location. The first configuration is considered to be the primary loading condition and it is used to select the sensors' configuration and to prove the accuracy of the shape sensing method. It consists of a concentrated force applied at the midpoint of the panel ($\frac{L}{2}; \frac{W}{2}$). The force has a module of 1000 N and is applied on the flat side of the skin along the z direction. The second configuration is considered to be an accidental loading condition that the method is challenged to solve even though it has been optimised for the primary condition only. It is used to assess the robustness of the method to unexpected deformations. It is obtained by moving the concentrated force

Table 1
Lamina characteristics.

E_{11} [GPa]	E_{22} [GPa]	ν_{12}	$G_{12} = G_{23} = G_{13}$ [GPa]	Thickness [mm]	ρ [kg/mm^3]
111	7.857	0.34	3.292	0.2	1.5E-06

Table 2
Composites' stacking sequences.

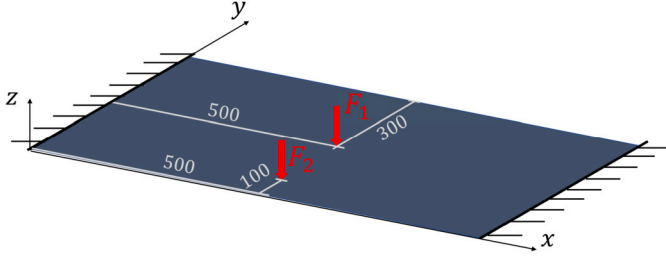| Component	St. Sequence	Total thickness [mm]
Skin	$[45/-45/0/90/-45/45/-45/45]_s$	3.2
Stringers	$[45/-45/0/90]_s$	1.6

Fig. 5. Loading configuration - The figure shows the two loading schemes. F_1 identifies the primary loading configuration whereas F_2 identifies the accidental one.
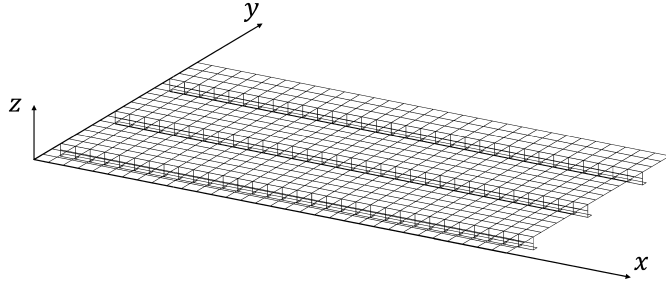

Fig. 6. Inverse mesh - This is the mesh used for the shape sensing with the iFEM.

closer to one edge of the panel. Fig. 5 shows the loading configurations on the panel.

4.2. Models and preliminary analysis

Two numerical models are used for the investigation. The first one is the model used for shape sensing with the iFEM. It is constituted by 928 iQS4 inverse elements whose detailed formulation is described in [40,43]. This model is shown in Fig. 6 and it will be defined as the *inverse mesh* in the rest of the paper.

The second model, defined as the *direct mesh*, is a more refined one, obtained from the inverse mesh by splitting each inverse element into nine direct elements. It is adopted to perform the static analysis under the loading configurations and for the computation of the modal characteristics of the structure. The input strains for the shape sensing and the deformed shape that need to be reconstructed are extracted from the static analysis of this model, analysed with the software MSC/NASTRAN®. For the inverse and the direct meshes, the normals of the elements are concordant with the z-axis and y-axis, for the elements aligned with the x-y and x-z planes, respectively.

The deformed shape for the primary loading condition from the static analysis of the direct mesh is presented in Fig. 7. This deformed shape is the one that the shape sensing methods are tested on. The first 30 modes of the structure are computed from the modal analysis of the direct mesh. Out of these 30 modes, those that mostly contribute to represent the primary static deformation are selected. The selection is
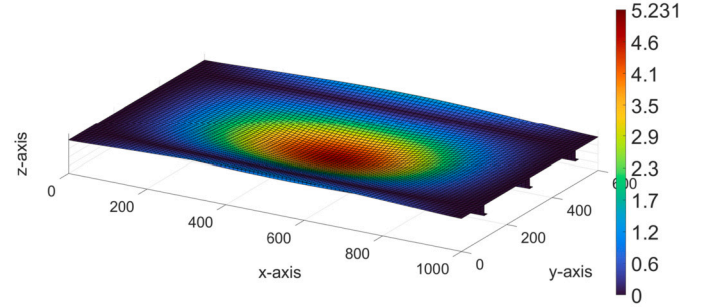

Fig. 7. Primary deformed shape - This is the primary deformed shape that the shape sensing methods is optimised to solve (all dimensions are expressed in mm).
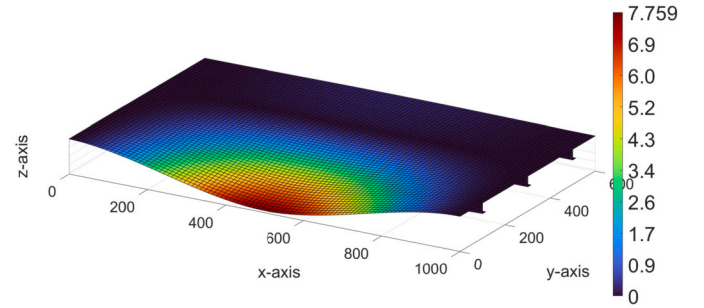

Fig. 8. Accidental deformed shape - This is the deformed shape that the robustness of the shape sensing methods is tested on (all dimensions are expressed in mm).

made by computing the percentage strain energy contribution of each mode to the total strain energy of the primary static deformation [28]. The first 29 modes contribute a 95% of the total strain energy and they are selected for the application of the MM and of the Modal VSE. It is important to highlight once again that the accidental deformation is not considered in this selection process at all. On the other hand, the accidental deformed shape, used to assess the robustness of the methods to unexpected deformations, is shown in Fig. 8.

5. Numerical results

5.1. Error assessment

The evaluation of the accuracy of the shape sensing is assessed through the computation of two errors. Since the predominant displacement of the deformed shape is the transverse one, along the z direction, the errors are computed with respect to this component. The first error considered is a local one. It is the percentage error on the reconstruction of the maximum transverse displacement experienced by the panel, $\%Err_w^{max}$. The second error takes into account the global accuracy of the reconstruction over the 990 nodes of the inverse mesh. It is the percentage root mean square error computed as follows:

$$\%Erms_w = 100 \times \sqrt{\frac{1}{990} \sum_{i=1}^{990} \left(\frac{w_i - w_i^{ref}}{w_{max}^{ref}} \right)^2} \tag{16}$$

where, w_i are the reconstructed transverse displacements, w_i^{ref} are the reference transverse displacements, computed from the analysis of the
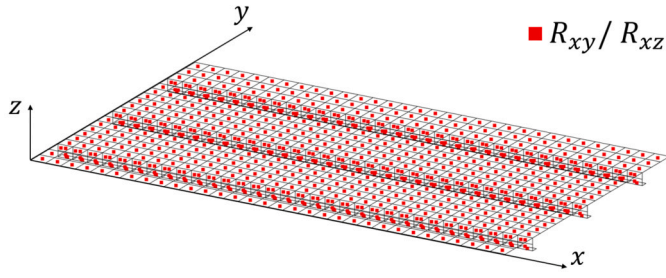
Fig. 9. Full set of sensors - The panel is equipped with strain rosettes in every centroid location of the inverse mesh. The rosettes measure the strain along x, y and x-y for the skin and the cap of the stringers ($\mathbf{R_{xy}}$). They measure the strain along x, z and x-z for the web of the stringers ($\mathbf{R_{xz}}$).

Fig. 11. Reduced set of sensors - The panel is equipped with strain rosettes in 70 centroid locations of the inverse mesh. Only rosettes on the skin are considered and they measure the strain along x, y and x-y ($\mathbf{R_{xy}}$).

Table 3
Results of the preliminary analysis on the reconstruction of the deformed shape of the primary loading condition.

Sensor conf.	MM		iFEM	
	$\%Err_w^{max}$	$\%Erms_w$	$\%Err_w^{max}$	$\%Erms_w$
Full set (Fig. 9)	6.2	1.1	0.3	0.1
Reduced set (Fig. 11)	9.2	2.2	67.4	23.2

direct mesh, and w_{max}^{ref} is the maximum value of the reference transverse displacements.

5.2. Preliminary computations

The primary deformed shape in Fig. 7 is particularly significant for this application and it is the only one considered for the preliminary computations described in this section. In fact, it highlights the limitations of the iFEM and the MM that are meant to be overcome by the formulation proposed in this work.

To highlight the behaviour of the methods, at first, the full set of strain sensors is considered, i.e. strain rosettes in a back-to-back configuration located at the 928 locations showed in Fig. 9, accounting for a total of 1856 sensors (considering that, for every location, the back-to-back configuration requires two sensors). In this case, the results relative to the primary deformed shape, in terms of $\%Err_w^{max}$ and $\%Erms_w$, obtained by the iFEM and the MM, are reported in Table 3. Moreover, Fig. 10 shows the distribution over the entire mesh of the error on the reconstruction of the traverse deflection computed for the i-th node:

$$\%Ew_i = 100 \times \left(\frac{|w_i - w_i^{ref}|}{|w_{max}^{ref}|} \right) \tag{17}$$

where the notation is the same adopted for Eq (16). When analysing the figures and the table, it is important to consider that the maximum of $\%Ew_i$ could be located in a different location than the one where the maximum transverse displacement (w_{max}^{ref}) is experienced. Therefore, the

maximum of $\%Ew_i$ in the plots may differ from $\%Err_w^{max}$ in the table. The table and the figures show that the displacement reconstruction obtained with the MM is modest, especially considering that it is obtained using the maximum number of installable sensors. Moreover, the comparison with the extreme accuracy of the iFEM proves the excellent performance of the latest and the moderate one of the MM for this configuration.

When reducing the number of sensors to only 140 (70 sensors' locations in a back-to-back configuration), the situation is reversed. The reduced set of sensors is obtained considering 140 strain rosettes only on the skin of the panel. They are distributed over its area, trying to cover a broad portion of the domain and considering a higher concentration of sensors where the strains for the primary loading condition are higher (Fig. 11). From the results reported in Table 3 and Fig. 12, it is clear that the overall accuracy of MM, evaluated with the $\%Erms_w$ parameter, is influenced by the reduction in the amount of strain information, but still preserves a decent accuracy. On the contrary, the iFEM's accuracy becomes extremely poor. Looking at the $\%Err_w^{max}$, the same trend can be observed for the reconstructions of the maximum deflection.

The results of this preliminary study, where only the primary loading condition is studied and the sensor expansion is not yet considered, prove once again that the MM can achieve moderate accuracy with a small number of sensors. Nevertheless, this accuracy seems to have an asymptotic value, impossible to exceed, even heavily increasing the number of sensors. They also confirm the extreme accuracy of the iFEM, but also the necessity of a considerable amount of sensors for the method to achieve this level.

5.3. Results after the virtual sensor expansion

The results from the preliminary computation inspired the formulation of the proposed mixed approach, aimed at combining the positive characteristics of the MM and the iFEM in order to overcome their individual limitations. The challenge is to exceed the accuracy of the MM
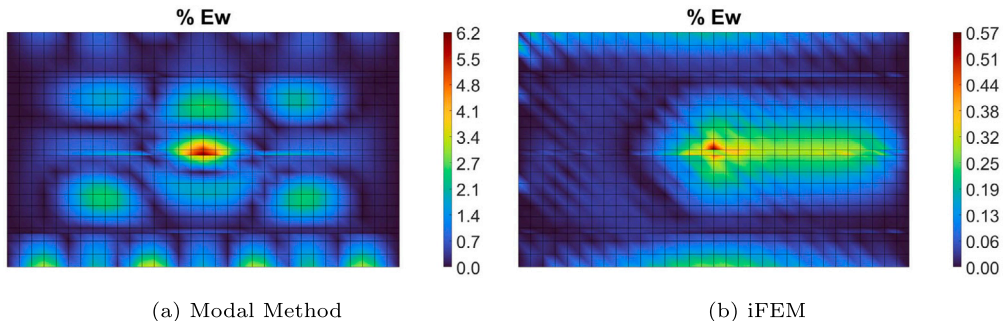

(a) Modal Method

(b) iFEM

Fig. 10. Shape sensing for the primary loading condition with the full set of sensors - Bottom view of the panel showing the distribution of the $\%Ew_i$ errors for the Modal Method and the iFEM.
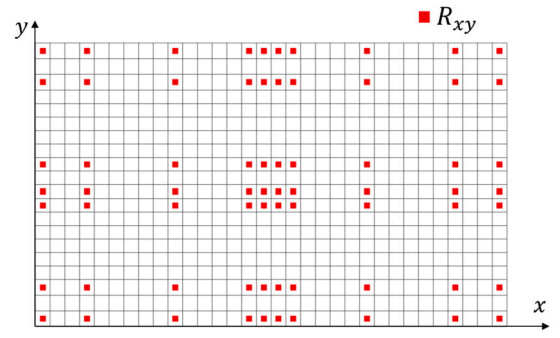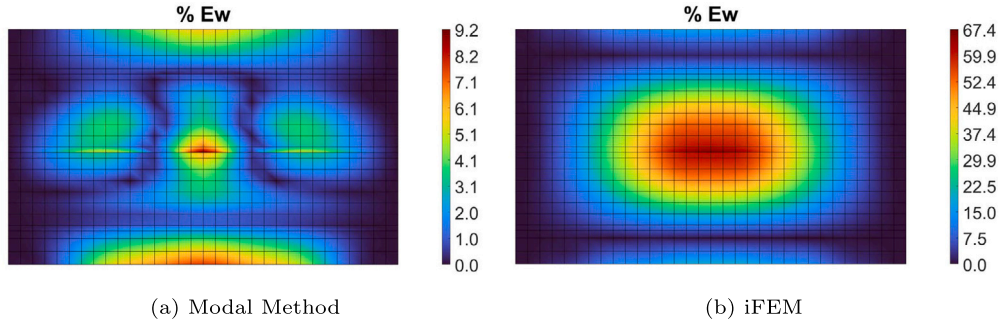
Fig. 12. Shape sensing with the reduced set of sensors - Bottom view of the panel showing the distribution of the $\%Ew_i$ errors for the MM and the iFEM.
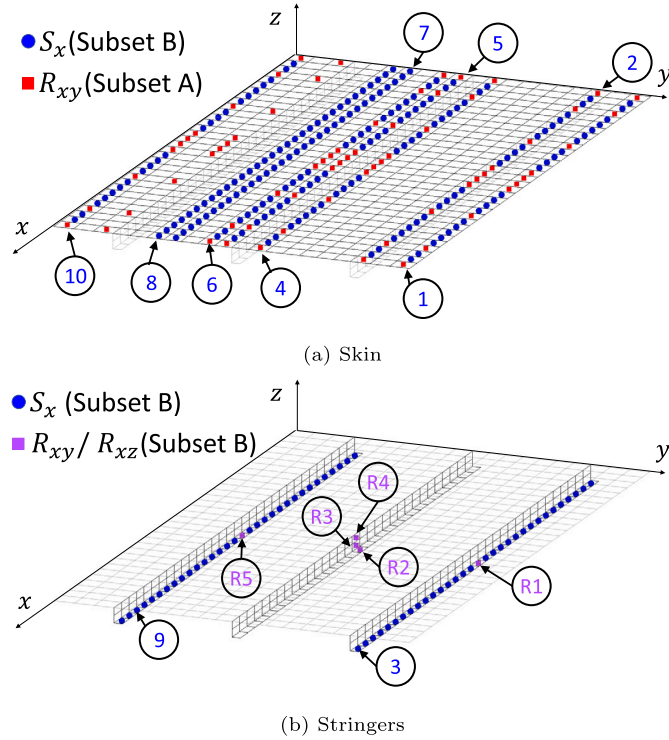

Fig. 13. Expanded set of sensors - The strain rosettes of subset A are illustrated by red squares. The 10 sensing lines along x and the 5 strain rosettes of subset B are indicated using labels from 1-10 and R1-R5, respectively. The configuration includes the back-to-back locations of 70 rosettes on the skin (■ R_{xy}/R_{xz}), 258 mono-directional strain gauges along x (● S_x) and 5 strain rosettes on the stringers (■ R_{xy}/R_{xz}).

when using only 140 sensors by virtually expanding them to feed the iFEM with sufficient strain information. The virtual expansion is obtained by the formulation introduced in Eq. (15).

To achieve this goal, the sensor configuration in Fig. 11, is expanded in order to include a sufficient amount of sensors for the iFEM. The expanded set of sensors is shown in Fig. 13. It includes the 140 strain rosettes of the reduced set (Fig. 11), where all membrane strains (ε_1, ε_2, ε_3) and bending curvatures (ε_4, ε_5, ε_6) are computed. This subset of sensors will be defined as **subset A**. In addition, the configuration includes 10 sensing lines along the x-axis of the panel, where ε_{xx}^+ and ε_{xx}^- are computed, and 5 sensing locations on the stringers, where all membrane strains (ε_1, ε_2, ε_3) and bending curvatures (ε_4, ε_5, ε_6) are computed. This subset of sensors is defined as **subset B**. To summarise, this configuration includes 258 mono-axial strain gauges (S_x) and 75 strain rosettes (R_{xy}/R_{xz}), all in a back-to-back configuration, thus accounting for a total of 666 sensors. This configuration is designed considering

the information and results already existing in the literature about the optimal sensing configurations for similar structures subjected to loading conditions similar to the primary one [43,44]. In fact, when using this set of sensors, without any application of VSE and thus considering that the sensors from subsets A and B are all actually measured, the iFEM is able to accurately reconstruct the deformed shape of the structure for the primary loading condition. The results of this analysis are reported in the first row of Table 4 and in Fig. 14a. The reconstructions of the iFEM for this case are not as accurate as the ones obtained with the full set of sensors, but they are consistently more accurate than the ones obtained by the MM and the iFEM when considering the reduced set of sensors. In fact, $\%Err_w^{max}$ and $\%Erms_w$ are more or less halved when compared with the MM (Table 3).

The next step is to analyse what happens when we actually measure only the strains coming from the reduced set of sensors and we virtually expand them according to the formulation introduced in Eq. (15). In this case, we define ε^m as the vector of the strains from the subset A in Fig. 13, whereas the vector ε^e is computed and contains the virtually expanded strains of subset B. The Φ_s^m and Φ_s^e matrices contain the modal strain shapes of the measured strain components and the expanded ones, respectively. Also, in this case, the first 29 strain shapes are considered. When considering this configuration, out of 666 sensors of the reduced set, only the 140 rosettes of the subset A are actually measured. When applying the iFEM, fed by the measured and virtually extrapolated strains, the results of the shape sensing for the primary loading condition are reported in the second row of Table 4 and in Fig. 14b. The procedure shows an $\%Err_w^{max} = 4.4$ and an $\%Erms_w = 1.1$. These values prove a good accuracy that is strongly comparable with the one shown by the iFEM when actually measuring the strains from the sensors of subsets A and B, without any VSE, thus demonstrating the convergence of the procedure to the solution obtained using the nominal strains. Moreover, considering the same actually measured sensors, both errors are, once again, halved with respect to the MM. In fact, it is important to highlight once again that these results are obtained by only measuring the strains from the 140 sensors in Fig. 11, which are extrapolated to obtain the sensor configuration in Fig. 13. In Table 4, the errors in the reconstructions of the two bending curvatures, θ_x and θ_y are also reported. These quantities also show that the introduction of the VSE does not compromise the accuracy of the reconstructions, which show comparable values with respect to the configuration with nominal strains. The analysis of Fig. 14b also proves the accuracy of the procedure. In fact, the plot shows that the distribution of $\%Ew_i$ on the panel never exceeds 5%. Only on one edge of the panel there is a local inaccuracy that does not appear in the reconstruction of Fig. 14a. Nevertheless, this local phenomenon is within the 5% threshold and does not compromise the overall accuracy of the procedure. In conclusion, in terms of displacement reconstruction, the proposed procedure is able to exceed the accuracy of the MM and reach the accuracy of the iFEM, fed with a sufficient number of sensors, but using a strongly reduced set of actually measured sensors.
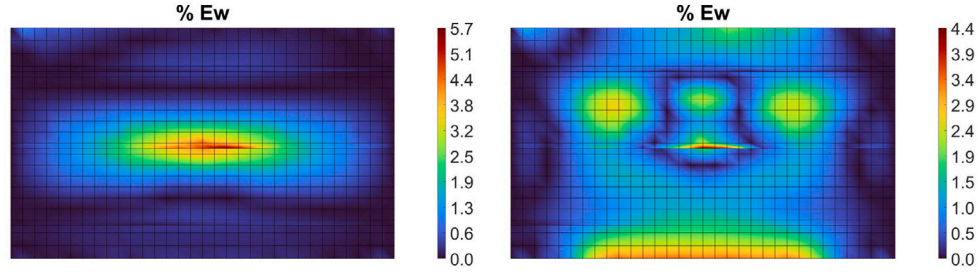
(a) iFEM with sensors from subsets A and B actually measured

(b) iFEM with sensors from subset A actually measured and sensors from subset B virtually expanded

Fig. 14. Shape sensing for the primary loading condition with the expanded set of sensors - Bottom view of the panel showing the distribution of the $\%Ew_i$ errors for the iFEM.

Table 4
Primary loading condition - Results for the expanded set of sensors. In the first row are reported the errors when using all measured strains from subsets A and B, whereas in the second row are reported the errors when using the combination of measured strains from subset A and virtually expanded strains from subset B.

	iFEM					
Sensors' conf.	$\%Err_w^{max}$	$\%Erms_w$	$\%Err_{\theta_x}^{max}$	$\%Erms_{\theta_x}$	$\%Err_{\theta_y}^{max}$	$\%Erms_{\theta_y}$
Subset A = measured; subset B = measured	4.8	1.1	1.46	3.80	5.02	1.28
Subset A = measured; subset B = virtual	4.4	1.1	-0.27	5.23	4.44	3.44

(a) ε_{xx}^+
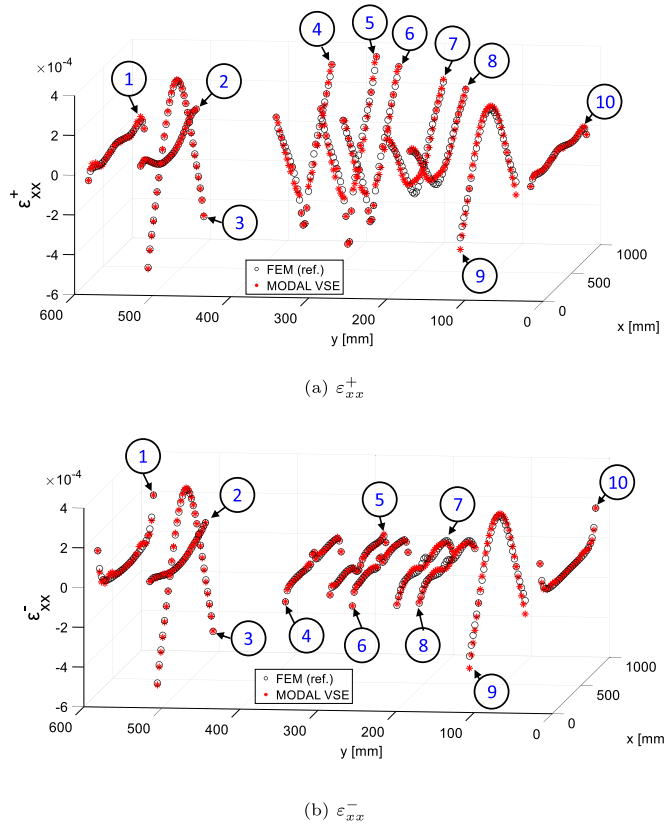

(b) ε_{xx}^-

Fig. 15. Virtual strain expansion - The figure shows the distributions of the nominal (FEM (ref.)) and extrapolated (MODAL VSE) strains over the area of the panel. The following components are plotted: ε_{xx}^+ (a), ε_{xx}^- (b).

To assess the effectiveness of the proposed procedure, it is also important to verify the method's accuracy for the extrapolation of the strains. The parameter used to assess the accuracy of the extrapolation is, once again, the root mean square percentage error defined as follows:

$$\%Erms_\varepsilon = 100 \times \sqrt{\frac{1}{N}\sum_{i=1}^{N}\left(\frac{\varepsilon_i - \varepsilon_i^{ref}}{\varepsilon_{max}^{ref}}\right)^2} \tag{18}$$

where the ε_i is the i-th strain component from the entire expanded set of sensors, ε_i^{ref} is the correspondent i-th nominal strain component computed through the static analysis of the direct mesh and ε_{max}^{ref} is the maximum value of the N ε_i^{ref} strain components. For the case study proposed here, the value of the error is small, $\%Erms_\varepsilon = 4.3$. In Fig. 15, the extrapolated strains, compared with the nominal strains, are plotted for the 10 sensing lines previously defined. The figure and the value of $\%Erms_\varepsilon$ show that over the area of the panel, the extrapolation of the strains is globally accurate. On lines 7 and 8, close to the maximum values of the deformation, the extrapolation presents some inaccuracies. These sensing lines do not have measured strains on them and, therefore are more difficult to extrapolate. This behaviour can be observed more in detail for line num. 8 in Fig. 16a. Also, the analysis of lines 3 and 9 requires further attention. These sensing lines, which are located on the stringers, lay outside of the plane of the skin of the panel, where the measured strains are located. This condition represents an unfeasible problem for other strain extrapolating methods (i.e., Smoothing Element Analysis, Polynomial extrapolation). Fig. 16b shows the extrapolation of ε_{xx}^+ for line 3. It proves that the proposed method is able to reconstruct these strains, which are impossible to extrapolate with other methods, with impressive accuracy. The result is even more impressive when considering that no measured sensor is located on the considered line.

The same condition applies to the strain rosettes included in the expanded set of sensors (Fig. 13b). Since they are located on the stringers of the panel, they also don't lay on the same plane as the measured strains. Fig. 17 shows the extrapolations of all three strain components for the 5 rosettes. The graphs demonstrate that the extrapolation of strains for rosettes number 1 and 5 is consistently accurate for all the strain components. On the contrary, the extrapolation of the strains from rosettes 2 and 3 is always incorrect and for rosette 4 only the ε_{xx}^+ and ε_{xx}^- components are precisely extrapolated.

Overall, the extrapolation of the strains shows good agreement with respect to the nominal ones, even in areas where the extrapolation is usually difficult or impossible. Some local inaccuracies are encountered
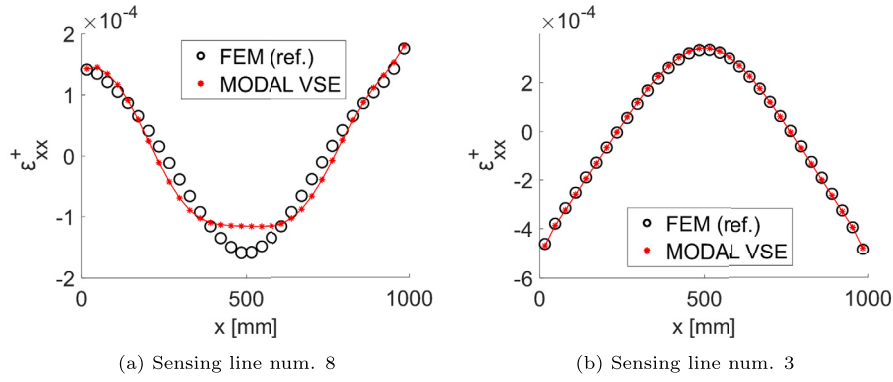
(a) Sensing line num. 8   (b) Sensing line num. 3

Fig. 16. VSE on sensing lines number 3 and 8 - The figures show the distributions of the nominal (FEM (ref.)) and the extrapolated (MODAL VSE) ε_{xx}^{+} along x for the sensing line number 8 (a) and 3 (b).

(a) ε_{xx}^{+} (b) ε_{yy}^{+} (c) γ_{xy}^{+}

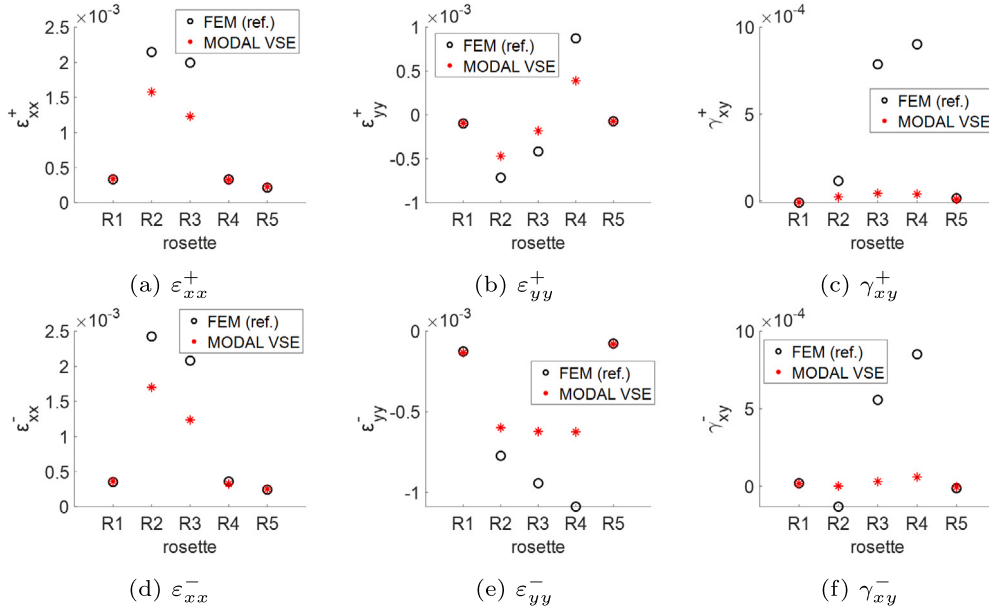(d) ε_{xx}^{-} (e) ε_{yy}^{-} (f) γ_{xy}^{-}

Fig. 17. Virtual strain expansion for rosettes - The figure shows the values of the nominal (FEM (ref.)) and extrapolated (MODAL VSE) strains for the 5 rosettes in Fig. 13b. The following components are plotted: ε_{xx}^{+} (a), ε_{yy}^{+} (b), γ_{xy}^{+} (c), ε_{xx}^{-} (d), ε_{yy}^{-} (e), γ_{xy}^{-} (f). For R3 and R4 the strain components are expressed in a local coordinate system that has the x-axis aligned with the global x and the y-axis aligned with the global z. The global axes are reported in Fig. 13.

for areas where no actually measured strains are located. These inaccuracies do not influence the reconstruction of the displacements with iFEM, which is as precise as the one obtained by using the nominal strains. This is due to the working principle of the iFEM. Since it relies on the least-square fitting of the input strains to compute the displacement fields, its formulation is able to smooth the influence of these outlying strains.

5.4. Results for the accidental loading condition

Another step of this work is to prove the robustness of the introduced procedure to a different deformation. For this purpose, the accidental loading condition has been introduced in Section 4.2. For this loading condition, neither the sensor configuration nor the modes for the Modal VSE have been specifically selected. It represents the case of a deformed shape experienced by the structure that is different from the one the monitoring system has been designed for. Therefore, no modification of the procedure is considered. For this test, the sensor configuration is the expanded one (Fig. 13). Also for this case, the first analysis is performed considering measured strains from the sensors subsets A and B. The values of the errors, reported in Table 5 are close to 1%, thus proving an efficient shape sensing of the deformation. However, in Fig. 18a,

it can be noticed that a local inaccuracy is present on one stringer of the structure, where $\%Ew_i$ reaches 6.7%. Nevertheless, considering that the sensors' configuration is not designed for this specific loading condition, despite this local phenomenon, it can be concluded that the iFEM shows satisfactory robustness to the change in the loading condition.

To finally prove the robustness of the process involving the Modal VSE combined with the iFEM, the procedure is tested on the accidental loading condition as well. The configuration is the same adopted for the primary loading condition and, consequently, the set of actually measured (subset A) and virtually expanded (subset B) strains is the one plotted in Fig. 13. The results of this analysis are reported in Table 5. The reconstruction of the displacements is satisfactory, with errors that do not exceed 3%. Also in this case the distribution of $\%Ew_i$ (Fig. 18b) shows a local peak on the same stringer of the previous case. Moreover, the errors relative to the bending rotations (Table 5) also show some high values for θ_x that are also present in the shape sensing with the nominal strains. Although this is not positive, it proves once again that this solution converges to the one obtained with the nominal strains, thus proving the efficiency and robustness of the Modal VSE+iFEM process. In fact, it can achieve the same accuracy, also for this accidental deformation, using only 140 actually measured sensors, virtually expanded to a total of 666 sensors.

Table 5

Accidental loading condition - Results for the expanded set of sensors. In the first row are reported the errors when using all measured strains from subsets A and B, whereas in the second row are reported the errors when using the combination of measured strains from subset A and virtually expanded strains from subset B.

Sensors' conf.	iFEM					
	$\%Err_w^{max}$	$\%Erms_w$	$\%Err_{\theta_x}^{max}$	$\%Erms_{\theta_x}$	$\%Err_{\theta_y}^{max}$	$\%Erms_{\theta_y}$
Subset A = measured; subset B = measured	0.9	1.1	8.93	8.52	-1.41	1.23
Subset A = measured; subset B = virtual	-2.9	1.2	13.25	10.95	1.94	3.36

(a) iFEM with sensors from subsets A and B actually measured

(b) iFEM with sensors from subset A actually measured and sensors from subset B virtually expanded
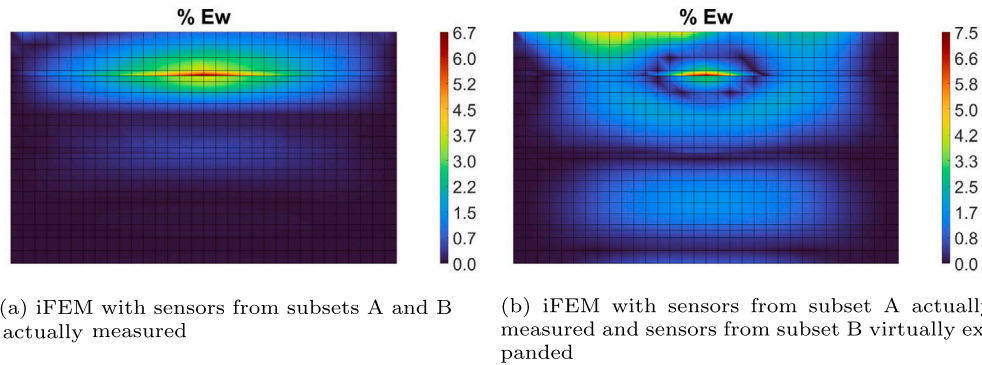
Fig. 18. Shape sensing for the accidental loading condition with the expanded set of sensors - Bottom view of the panel showing the distribution of the $\%Ew_i$ errors for the iFEM.
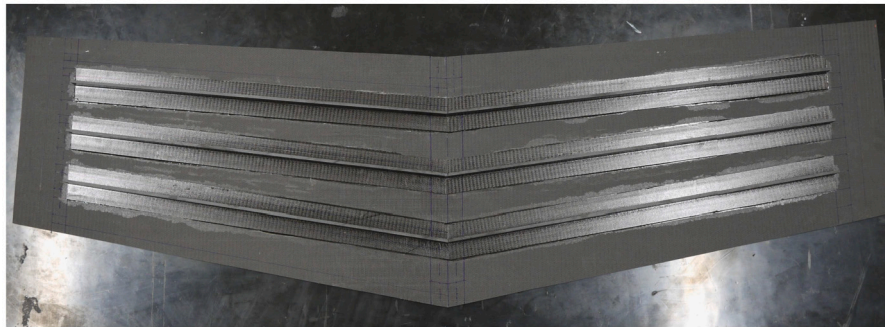

Fig. 19. Experimental wing-shaped composite panel.

Table 6

TWILL T-300 nominal properties.

E_{11} [GPa]	E_{22} [GPa]	v_{12}	$G_{12} = G_{23} = G_{13}$ [GPa]	Thickness [mm]	ρ [kg/mm^3]
59.7	59.7	0.09	3.8	0.25	1.5E-06

6. Experimental validation

6.1. Experimental test case

The experimental validation of the introduced methodology is performed on a composite wing-shaped panel (Fig. 19). The panel is stiffened with three T-section stringers on one side of the panel, whereas the other side is flat. The geometry of the experimental test case is illustrated in Fig. 20. The panel is made of a multilayered composite whose layers are made of a TWILL T-300 carbon-fibre fabric prepreg. The characteristics of the prepreg are reported in Table 6. The layup stacking sequence of the panel and of the stringers is $[45/0/0/45/0/0/0/45]_s$. From the described structure, an inverse model constituted of 960 iQS4 is derived (Fig. 21). A second high-fidelity model is also created to extract the first eighteen modal shapes of the structure for the application of the Modal VSE.

As for the numerical study, two loading conditions are considered to study the different behaviour of the MM, the iFEM and the introduced Modal VSE+iFEM formulation. Both the load cases have simply supported boundary conditions applied at the two tips of the wing shaped panel and a concentrated force applied at the root section of the wing. They differ in the application point of the load and the induced deformation. The **Load case 1** includes a transverse concentrated force, F_1, located at 106 mm from the trailing edge, as shown in Fig. 21. This loading condition induces a primary bending deformation with a small contribution from the torsional behaviour. On the other hand, the **Load case 2** includes a transverse concentrated load, F_2, that induces a combined deformation of bending and torsion.

The panel is instrumented with fibre optic distributed strain sensors based on the Rayleigh scattering and optical frequency domain reflectometry (OFDR). They are placed along the wing span of the panel, and the strain is measured along the laying direction of the fibre. By using two 10-meter-long fibres, the sensing of the strain in the centroid locations of the inverse mesh shown in Fig. 21 is experimentally obtained. In addition to the fibres, 8 locations are instrumented with strain rosettes
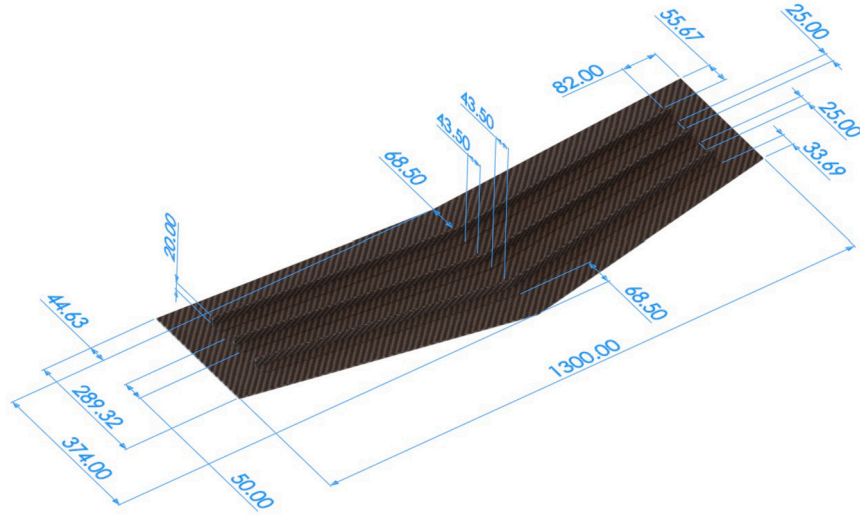
Fig. 20. Experimental wing-shaped panel's geometry - The figure shows the geometry of the experimental stiffened panel (all dimensions are expressed in mm).
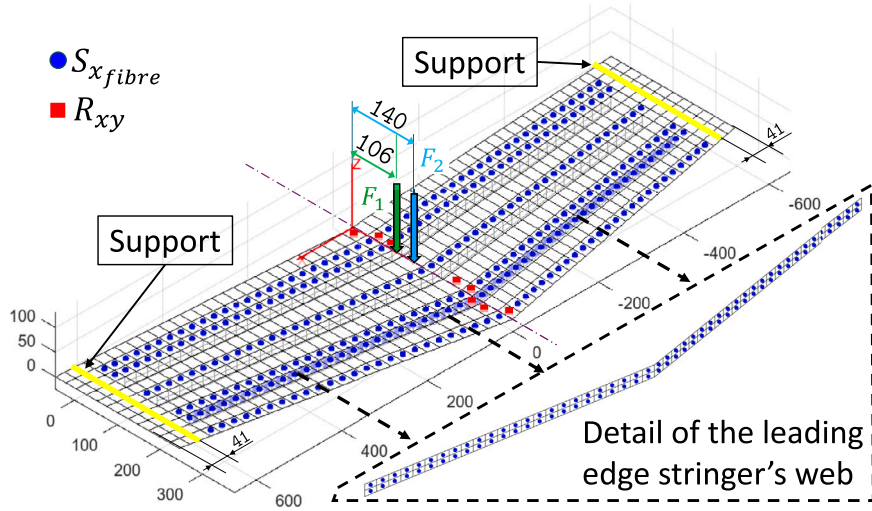

Fig. 21. Experimental wing-shaped panel's inverse mesh - The figure shows the inverse mesh of the panel, the loading configurations and the **full set** of experimental sensors. ($\bullet$ $S_{x_{fibre}}$) are the sensing locations of the fibres and ($\blacksquare$ R_{xy}) are the sensing locations of the strain rosettes (all dimensions are expressed in mm).
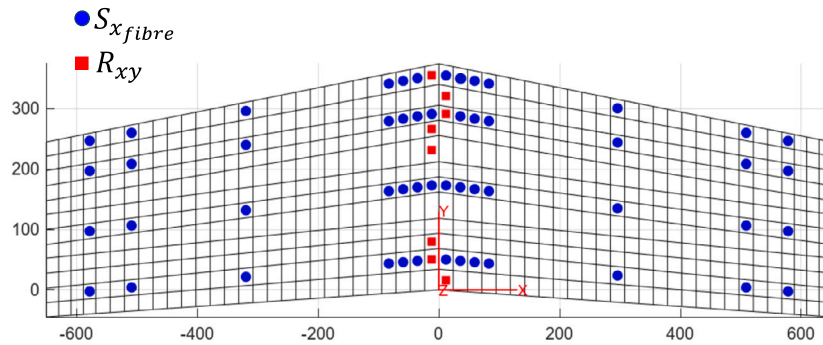

Fig. 22. Reduced set of experimental sensors - The figure shows the **reduced set** of experimental sensors. ($\bullet$ $S_{x_{fibre}}$) are the sensing locations of the fibres and ($\blacksquare$ R_{xy}) are the sensing locations of the strain rosettes (all dimensions are expressed in mm).

(Fig. 21). As in the previous numerical application, also in this case, the configuration considers back-to-back sensors. To summarise, the experimental configuration of sensors consists of 780 strain measurements coming from the fibres and 48 coming from the strain rosettes, accounting for a total of 828 measured strains. This configuration represents the **full set** of the experimental sensors.

From this full set, a **reduced set** is extracted, following the instructions on the distribution of sensors provided by the numerical study. The **reduced set** preserves the rosettes of the full set but consists of a strongly reduced number of strain measurements from the fibres. The distribution of the sensors is shown in Fig. 22. The configuration is clearly inspired by the one shown in Fig. 11 for the numerical appli-
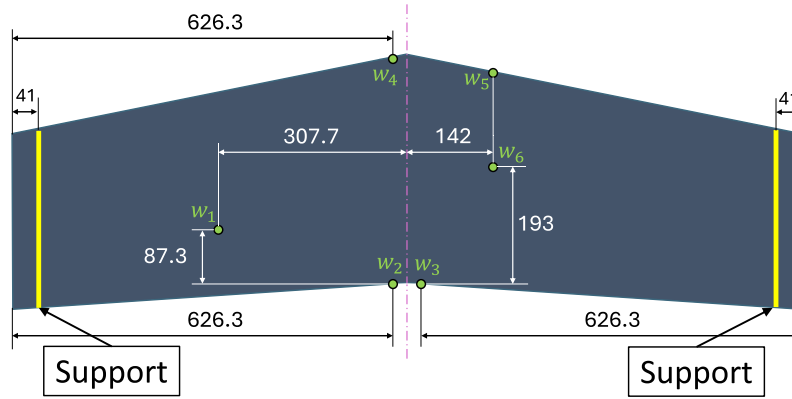
Fig. 23. Displacement sensors - The figure shows the configuration of the six transverse displacement sensors w_{1-6} (all dimensions are expressed in mm).
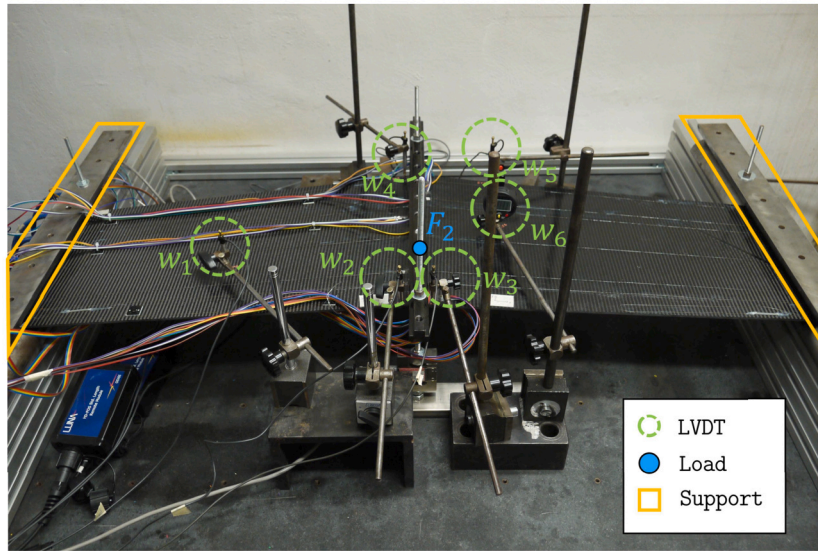

Fig. 24. Experimental configuration - The figure shows the testing configuration for the wing-shaped composite panel.

cation. Moreover, in the context of the application of the Modal VSE, it is important to highlight once again that the **reduced set** does not include sensors on the stiffeners of the panel, that are present in the **full set**. This reduced set consists of 106 strain measurements coming from the fibres and 48 coming from the strain rosettes, accounting for a total of 154 measured strains. Therefore, the **reduced set** diminishes the considered strain measurements by 81% with respect to the **full set**.

The experimental set-up is completed with the sensors that measure the experimental displacements, which are used as a reference for assessing the accuracy of the shape sensing. During the test, the panel is equipped on the flat surface with six LVDTs, as illustrated in Fig. 23. They measure the transverse displacements in six randomly distributed locations over the area of the panel, thus giving information on the overall deformation of the structure.

6.2. Experimental results

The experimental test is performed by loading the structure on the test bench illustrated in Fig. 24. More detail on the testing configuration can be found in [44]. For both loading conditions, a load of 200 N is applied. During the tests, the data from all the sensors are collected. Several analyses are performed based on these data.

The first analysis simply considers the application of the standard iFEM when the **full set** of strain sensors are included. Table 7 shows the results of this analysis in terms of reconstructed transverse displacements and percentage errors with respect to the measured ones. As

Table 7
Results when the **full set** of measured sensors is considered: the experimentally measured and the reconstructed transverse displacements are reported for the two load cases. In parentheses, the percentage errors with respect to the experimental values are reported. Moreover, the mean of the absolute value of the percentage error is also reported ($\mu(|\%Err|)$).

	Load case 1		Load case 2	
	Experimental	iFEM	Experimental	iFEM
$F\ [N]$	200		200	
$w_1\ [mm]$	2.44	2.55	2.42	2.50
$(\%Err_{w_1})$		(+4.2%)		(+3.5%)
$w_2\ [mm]$	3.72	3.89	2.98	3.14
$(\%Err_{w_2})$		(+4.5%)		(+5.2%)
$w_3\ [mm]$	3.72	3.90	2.98	3.14
$(\%Err_{w_3})$		(+4.8%)		(+5.4%)
$w_4\ [mm]$	3.77	3.51	5.18	4.84
$(\%Err_{w_4})$		(-7.0%)		(-6.5%)
$w_5\ [mm]$	3.42	3.19	4.72	4.35
$(\%Err_{w_5})$		(-6.8%)		(-8.0%)
$w_6\ [mm]$	3.29	3.36	3.75	3.82
$(\%Err_{w_6})$		(+1.9%)		(+1.8%)
$\mu(|\%Err|)$		4.9%		5.1%

already demonstrated by past studies and by the previously described numerical study, the iFEM show high accuracy when a consistent num-

Table 8

Results when the **reduced set** of measured sensors is considered: the experimentally measured and the reconstructed transverse displacements are reported for the two load cases. In parentheses, the percentage errors with respect to the experimental values are reported. Moreover, the mean of the absolute value of the percentage error is also reported ($\mu(|\%Err|)$).

	Load case 1			Load case 2		
	Experimental	iFEM	MM	Experimental	iFEM	MM
$F\ [N]$	200			200		
$w_1\ [mm]$	2.44	0.78	2.40	2.42	0.72	2.35
($\%Err_{w_1}$)		(-68.0%)	(-1.8%)		(-70.1%)	(-2.6%)
$w_2\ [mm]$	3.72	1.55	3.84	2.98	1.37	2.95
($\%Err_{w_2}$)		(-58.3%)	(+3.3%)		(-54.1%)	(-1%)
$w_3\ [mm]$	3.72	1.55	3.84	2.98	1.36	2.98
($\%Err_{w_3}$)		(-58.2%)	(+3.3%)		(-54.2%)	(0.0%)
$w_4\ [mm]$	3.77	1.58	3.98	5.18	1.60	6.38
($\%Err_{w_4}$)		(-58.0%)	(+5.7%)		(-69.2%)	(+23.3%)
$w_5\ [mm]$	3.42	1.29	3.60	4.72	1.26	5.67
($\%Err_{w_5}$)		(-62.2%)	(+5.2%)		(-73.4%)	(+20.1%)
$w_6\ [mm]$	3.29	1.19	3.31	3.75	1.11	3.64
($\%Err_{w_6}$)		(-63.7%)	(+0.7%)		(-70.5%)	(-2.9%)
$\mu(|\%Err|)$		61.4%	3.3%		65.3%	8.3%

Table 9

Results when the **reduced set** of measured sensors is virtually expanded to the **full set**: the experimentally measured and the reconstructed transverse displacements are reported for the two load cases. In parentheses, the percentage errors with respect to the experimental values are reported. Moreover, the mean of the absolute value of the percentage error is also reported ($\mu(|\%Err|)$).

	Load case 1		Load case 2	
	Experimental	Modal VSE+iFEM	Experimental	Modal VSE+iFEM
$F\ [N]$	200		200	
$w_1\ [mm]$	2.44	2.40	2.42	2.33
($\%Err_{w_1}$)		(-1.7%)		(-3.4%)
$w_2\ [mm]$	3.72	3.86	2.98	2.73
($\%Err_{w_2}$)		(+3.8%)		(-8.3%)
$w_3\ [mm]$	3.72	3.87	2.98	2.74
($\%Err_{w_3}$)		(+4.0%)		(-8.1%)
$w_4\ [mm]$	3.77	3.77	5.18	5.06
($\%Err_{w_4}$)		(-0.1%)		(-2.3%)
$w_5\ [mm]$	3.42	3.42	4.72	4.58
($\%Err_{w_5}$)		(-0.0%)		(-3.0%)
$w_6\ [mm]$	3.29	3.28	3.75	3.46
($\%Err_{w_6}$)		(-0.4%)		(-7.8%)
$\mu(|\%Err|)$		1.7%		5.5%

ber of sensors are available. In fact, the percentage errors never exceed 8% for both load cases, and the mean absolute error is close to 5%.

The second analysis only considers the measured data from the **reduced set** of sensors, without any strain pre-extrapolation. The results of this analysis are reported in Table 8. When applying the iFEM and the MM with this reduced set of strain information, they show different behaviour. The iFEM clearly struggles to reconstruct the transverse displacements correctly, with errors that reach more than 65% for both load cases. On the other hand, the MM is able to reconstruct the deformed shape more accurately. In particular, the simple bending load case (**Load case 1**) shows very accurate reconstructions, with a mean error of 3.3%. However, for the more complex loading condition, that involves a consistent amount of torsion (**Load case 2**), the errors reach more than 20% for the highest and most relevant displacements (w_4, w_5). The formulation introduced in the present work aims at tackling the problem related to these complex deformations, where MM struggles to give accurate reconstructions and iFEM requires too many sensors.

The last analysis introduces the Modal VSE combined with iFEM for the experimental test case. For this configuration, the data from the **resuced set** are the only ones actually measured from the sensors, as for the second analysis. However, this time, these data are used as master strains to virtually retrieve all the strains from the **full set** of sensors,

through the Modal VSE procedure. Thanks to this procedure, the number of measured sensors is 81% less with respect to the full set. By feeding these virtually expanded strains to the iFEM, the results shown in Table 9 are obtained. These results demonstrate that the proposed formulation is able to guarantee a high level of accuracy for the two load cases. In particular, the most difficult deformation, relative to **Load case 2**, is reconstructed with the same accuracy as the first analysis, where all the sensors of the full set were actually measured. The mean absolute per cent error is 5.1%, and the maximum is −8.3%. In addition, for **Load case 1**, the expansion of the reduced set does not perturb the excellent results already obtained by the MM with the reduced set of sensors. In this case, the mean absolute per cent error is 1.7%, and the maximum is +3.8%. The conclusions of this experimental activity confirm the results of the numerical study. The Modal VSE, coupled with the iFEM, is able to simultaneously overcome the limitations of the iFEM and MM for complex load cases by allowing very accurate displacement reconstruction with a strongly reduced number of sensors.

7. Conclusions

In this work, a method to strongly reduce the number of necessary strain sensors for the accurate shape sensing of a structure is proposed.

The method is inspired by the performances of two existing shape sensing methods, the inverse Finite Element Method and the Modal Method. In fact, the MM has proven to be moderately accurate when sparse sensor configurations are available, whereas the iFEM can exceed this accuracy when a sufficient amount of sensors are available. The proposed procedure is meant to combine the strengths of the two formulations to overcome their limitations when adopted separately and to obtain an efficient shape sensing method with sparse sensor configurations.

The introduced method consists of a preliminary virtual sensor expansion process, obtained through a formulation based on the MM. This process expands the strain information coming from a few sensors using the modal strain shapes of the structure. The expanded set of strains is then used to perform the shape sensing with the most accurate method, the iFEM.

The new procedure is firstly tested on the numerical shape sensing of a multilayered composite stiffened panel. Two different loading conditions are considered, the first one being the one expected by the structure and the one used to design the testing configuration, the second one being an accidental condition used to test the effectiveness and robustness of the procedure on a loading condition different from the primary one. The preliminary analysis of the structure once again highlighted the strengths and the limitations of the two shape sensing methods and the need for a considerable amount of sensors to get accurate displacement reconstructions. For both loading configurations, the introduction of the Modal Virtual Sensor Expansion coupled with the iFEM is proven to be able to overcome the limitations of the MM and iFEM. In fact, for the specific cases, the virtual expansion of a set of only 140 actually measured strain sensors to a set of 666 ones allows to obtain a level of accuracy in the shape sensing that is comparable to the one reached with 666 actually measured sensors, thus reducing the number of required sensors by 79%. Moreover, the Modal VSE shows an overall consistent effectiveness in the extrapolation of the strains, even for portions of the structure not equipped with actually measured sensors.

The numerical results are then experimentally validated on the shape sensing of a composite wing-shaped stiffened panel. Also, in this case, two loading conditions are considered. The experimental campaign confirms the results of the numerical investigation. The introduction of the new formulation is able to reduce the number of measured strains by 81%, without compromising the accuracy of the displacements' reconstructions.

In conclusion, the introduced method is able to strongly reduce the number of strain information required for accurate shape sensing. Nevertheless, the number of reduced sensors for the considered applications is still considerable. For this reason, although the introduced formulation represents a big step forward, future work should focus on the further reduction of strain sensors by means of detailed optimisations of the sensor configurations coupled with the Modal VSE and iFEM. Moreover, the adoption of the Modal VSE introduces a parameter that influences the accuracy of the strain pre-extrapolations, which is the selection of modes to retain in the expansion. In this work, a selection criterion based on the expected deformation of the structure, which is not always known, is adopted. By analysing different load cases, this work proves that the selection criteria can also be robust for deformations different from the one directly used for the selection. However, in some cases, the expected deformation can not be inferred at all. Future work should investigate selection criteria for the modes that do not require any knowledge of the expected deformation.

CRediT authorship contribution statement

Marco Esposito: Writing – review & editing, Writing – original draft, Visualization, Validation, Supervision, Software, Resources, Methodology, Investigation, Formal analysis, Data curation, Conceptualization.

Declaration of competing interest

The authors declare that they have no known competing financial interests or personal relationships that could have appeared to influence the work reported in this paper.

Data availability

Data will be made available on request.

References

[1] Colombo L, Sbarufatti C, Giglio M. Definition of a load adaptive baseline by inverse finite element method for structural damage identification. Mech Syst Signal Process 2019;120:584–607. https://doi.org/10.1016/j.ymssp.2018.10.041.

[2] Roy R, Gherlone M, Surace C, Tessler A. Full-field strain reconstruction using uniaxial strain measurements: application to damage detection. Appl Sci 2021;11(4). https://doi.org/10.3390/app11041681.

[3] Li M, Kefal A, Cerik BC, Oterkus E. Dent damage identification in stiffened cylindrical structures using inverse finite element method. Ocean Eng 2020;198:106944. https://doi.org/10.1016/j.oceaneng.2020.106944.

[4] Colombo L, Oboe D, Sbarufatti C, Cadini F, Russo S, Giglio M. Shape sensing and damage identification with ifem on a composite structure subjected to impact damage and non-trivial boundary conditions. Mech Syst Signal Process 2021;148:107163. https://doi.org/10.1016/j.ymssp.2020.107163.

[5] Airoldi A, Sala G, Evenblij R, Koimtzoglou C, Loutas T, Carossa GM, et al. Load monitoring by means of optical fibres and strain gages. In: Wölcken PC, Papadopoulos M, editors. Smart intelligent aircraft structures (SARISTU). Cham: Springer International Publishing; 2016. p. 433–69.

[6] Nakamura T, Igawa H, Kanda A. Inverse identification of continuously distributed loads using strain data. Aerosp Sci Technol 2012;23(1):75–84. https://doi.org/10.1016/j.ast.2011.06.012.

[7] Candon MJ, Esposito M, Levinski O, Joseph N, Koschel S, Carrese R, et al. On the application of a long-short-term memory deep learning architecture for aircraft transonic buffet loads monitoring. in: AIAA Scitech 2020 Forum. https://doi.org/10.2514/6.2020-0702.

[8] Kefal A, Diyaroglu C, Yildiz M, Oterkus E. Coupling of peridynamics and inverse finite element method for shape sensing and crack propagation monitoring of plate structures. Comput Methods Appl Mech Eng 2022;391:114520. https://doi.org/10.1016/j.cma.2021.114520.

[9] Barbarino S, Bilgen O, Ajaj RM, Friswell MI, Inman DJ. A review of morphing aircraft. J Intell Mater Syst Struct 2011;22(9):823–77. https://doi.org/10.1177/1045389X11414084.

[10] de Souza Siqueira Versiani T, Silvestre FJ, Guimarães Neto AB, Rade DA, Annes da Silva RG, Donadon MV, et al. Gust load alleviation in a flexible smart idealized wing. Aerosp Sci Technol 2019;86:762–74. https://doi.org/10.1016/j.ast.2019.01.058.

[11] Tessler A, Spangler JL. A variational principle for reconstruction of elastic deformations in shear deformable plates and shells. Report NASA/TM-2003-212445. Hampton, VA, United States: NASA Langley Research Center; 2003.

[12] Gherlone M, Cerracchio P, Mattone M, Sciuva MD, Tessler A. An inverse finite element method for beam shape sensing: theoretical framework and experimental validation. Smart Mater Struct 2014;23(4):045027. https://doi.org/10.1088/0964-1726/23/4/045027.

[13] Zhao F, Xu L, Bao H, Du J. Shape sensing of variable cross-section beam using the inverse finite element method and isogeometric analysis. Measurement 2020;158:107656. https://doi.org/10.1016/j.measurement.2020.107656.

[14] Roy R, Gherlone M, Surace C. A shape sensing methodology for beams with generic cross-sections: application to airfoil beams. Aerosp Sci Technol 2021;110:106484. https://doi.org/10.1016/j.ast.2020.106484.

[15] Papa U, Russo S, Lamboglia A, Core GD, Iannuzzo G. Health structure monitoring for the design of an innovative uas fixed wing through inverse finite element method (ifem). Aerosp Sci Technol 2017;69:439–48. https://doi.org/10.1016/j.ast.2017.07.005.

[16] Gherlone M, Cerracchio P, Mattone M. Shape sensing methods: review and experimental comparison on a wing-shaped plate. Prog Aerosp Sci 2018;99:14–26. https://doi.org/10.1016/j.paerosci.2018.04.001.

[17] Cerracchio P, Gherlone M, Tessler A. Real-time displacement monitoring of a composite stiffened panel subjected to mechanical and thermal loads. Meccanica 2015;50:2487–96. https://doi.org/10.1007/s11012-015-0146-8.

[18] Zhao F, Bao H, Liu J, Li K. Shape sensing of multilayered composite and sandwich beams based on refined zigzag theory and inverse finite element method. Compos Struct 2021;261:113321. https://doi.org/10.1016/j.compstruct.2020.113321.

[19] Kefal A, Tessler A, Oterkus E. An enhanced inverse finite element method for displacement and stress monitoring of multilayered composite and sandwich structures. Compos Struct 2017;179:514–40. https://doi.org/10.1016/j.compstruct.2017.07.078.

[20] Kefal A, Tabrizi I, Tansan M, Kisa E, Yildiz M. An experimental implementation of inverse finite element method for real-time shape and strain sensing of composite and

sandwich structures. Compos Struct 2021;258:113431. https://doi.org/10.1016/j.compstruct.2020.113431.

[21] Kefal A, Oterkus E. Isogeometric ifem analysis of thin shell structures. Sensors 2020;20(9). https://doi.org/10.3390/s20092685.

[22] Del Priore E, Lampani L. A methodology for applying isogeometric inverse finite element method to the shape sensing of stiffened thin-shell structures. Thin-Walled Struct 2024;199:111837. https://doi.org/10.1016/j.tws.2024.111837.

[23] Belur MY, Kefal A, Abdollahzadeh MA, Fassois SD. Damage diagnosis of plates and shells through modal parameters reconstruction using inverse finite-element method. Struct Health Monit 2024. https://doi.org/10.1177/14759217241249678.

[24] Ganjdoust F, Kefal A, Tessler A. A novel delamination damage detection strategy based on inverse finite element method for structural health monitoring of composite structures. Mech Syst Signal Process 2023;192:110202. https://doi.org/10.1016/j.ymssp.2023.110202.

[25] Foss G, Haugse E. Using modal test results to develop strain to displacement transformations. In: Proceedings of the 13th international modal analysis conference; 1995.

[26] Pisoni AC, Santolini C, Hauf DE, Dubowsky S. Displacements in a vibrating body by strain gauge measurements. In: Proceedings of the 13th international modal analysis conference; 1995.

[27] Li L, Zhong BS, Geng ZY, Sun W. Structural shape reconstruction of FBG flexible plate using modal superposition method. In: 29th conference on mechanical vibration and noise of international design engineering technical conferences and computers and information in engineering conference, vol. 8; 08 2017. V008T12A038.

[28] Bogert P, Haugse E, Gehrki R. Structural shape identification from experimental strains using a modal transformation technique. In: 44th AIAA/ASME/ASCE/AHS/ASC structures, structural dynamics, and materials conference; 2012.

[29] Freydin M, Rattner MK, Raveh DE, Kressel I, Davidi R, Tur M. Fiber-optics-based aeroelastic shape sensing. AIAA J 2019;57(12):5094–103. https://doi.org/10.2514/1.J057944.

[30] Drachinsky A, Freydin M, Raveh DE. Large deformation shape sensing using a non-linear strain to displacement method. AIAA J 2022;60(9):1–12. https://doi.org/10.2514/1.J061832.

[31] Soller BJ, Gifford DK, Wolfe MS, Froggatt ME. High resolution optical frequency domain reflectometry for characterization of components and assemblies. Opt Express Jan 2005;13(2):666–74. https://doi.org/10.1364/OPEX.13.000666.

[32] Di Sante R. Fibre optic sensors for structural health monitoring of aircraft composite structures: recent advances and applications. Sensors 2015;15(8):18666–713. https://doi.org/10.3390/s150818666.

[33] Esposito M, Gherlone M. Composite wing box deformed-shape reconstruction based on measured strains: optimization and comparison of existing approaches. Aerosp Sci Technol 2020;99:105758. https://doi.org/10.1016/j.ast.2020.105758.

[34] Esposito M, Gherlone M. Material and strain sensing uncertainties quantification for the shape sensing of a composite wing box. Mech Syst Signal Process 2021;160:107875. https://doi.org/10.1016/j.ymssp.2021.107875.

[35] Tessler A, Riggs H, Freese CE, Cook GM. An improved variational method for finite element stress recovery and a posteriori error estimation. Comput Methods Appl Mech Eng 1998;155(1):15–30. https://doi.org/10.1016/S0045-7825(97)00135-7.

[36] Kefal A, Tabrizi IE, Yildiz M, Tessler A. A smoothed ifem approach for efficient shape-sensing applications: numerical and experimental validation on composite structures. Mech Syst Signal Process 2021;152:107486. https://doi.org/10.1016/j.ymssp.2020.107486.

[37] Roy R, Tessler A, Surace C, Gherlone M. Efficient shape sensing of plate structures using the inverse finite element method aided by strain pre-extrapolation. Thin-Walled Struct 2022;180:109798. https://doi.org/10.1016/j.tws.2022.109798.

[38] Abdollahzadeh M, Tabrizi I, Kefal A, Yildiz M. A combined experimental/numerical study on deformation sensing of sandwich structures through inverse analysis of pre-extrapolated strain measurements. Measurement 2021;185:110031. https://doi.org/10.1016/j.measurement.2021.110031.

[39] Oboe D, Colombo L, Sbarufatti C, Giglio M. Comparison of strain pre-extrapolation techniques for shape and strain sensing by ifem of a composite plate subjected to compression buckling. Compos Struct 2021;262:113587. https://doi.org/10.1016/j.compstruct.2021.113587.

[40] Kefal A, Oterkus E, Tessler A, Spangler JL. A quadrilateral inverse-shell element with drilling degrees of freedom for shape sensing and structural health monitoring. Int J Eng Sci Technol 2016;19(3):1299–313. https://doi.org/10.1016/j.jestch.2016.03.006.

[41] Tessler A, Spangler JL. A least-squares variational method for full-field reconstruction of elastic deformations in shear-deformable plates and shells. Comput Methods Appl Mech Eng 2005;194(2):327–39. https://doi.org/10.1016/j.cma.2004.03.015.

[42] O'Callahan JC, Avitabile P, Riemer R. System equivalent reduction expansion process. In: Proc. of the 7th inter. modal analysis conf.; 1989.

[43] Esposito M, Mattone M, Gherlone M. Experimental shape sensing and load identification on a stiffened panel: a comparative study. Sensors 2022;22(3). https://doi.org/10.3390/s22031064.

[44] Esposito M, Roy R, Surace C, Gherlone M. Hybrid shell-beam inverse finite element method for the shape sensing of stiffened thin-walled structures: formulation and experimental validation on a composite wing-shaped panel. Sensors 2023;23(13). https://doi.org/10.3390/s23135962.